DE GRUYTER Open Physics 2025; 23: 20250195

Research Article

Mohamed M. Khader, Mohamed Adel*, and Mohamed Messaoudi

Numerical investigation of mixed convection and viscous dissipation in couple stress nanofluid flow: A merged Adomian decomposition method and Mohand transform

https://doi.org/10.1515/phys-2025-0195
received March 26, 2025; accepted July 04, 2025

Abstract: This work focuses on the impact of a magnetic field and viscous dissipation on the mixed convective flow of a couple stress nanofluid over a sheet that is stretching linearly. The research focuses on how these variables impact the model's overall heat transfer characteristics and the fluid's behavior. The sheet's stretching causes the fluid to move as it extends, which is what causes the flow. When considering a heating procedure at the prescribed surface temperature, the heat transmission problem has been examined. The modified Adomian decomposition method (ADM) is a computational method that simplifies the complex governing equations of the model under study and finds their numerical solutions. This technique uses the Mohand transform in conjunction with the ADM, which ensures a high degree of convergence, producing a series solution that closely resembles the exact solution to the problem. In addition, we evaluate the residual error function to satisfy the effectiveness and accuracy of the introduced technique. When the current findings were compared with other methods for particular flow scenarios, they demonstrated strong agreement, confirming the accuracy of the solution. A complete examination of the effects of the different parameters has been provided, including graphic and tabular illustrations of the effects. Additionally, a comparison chart illustrating the agreement between the two sets of data has been given to show the coherence between the present numerical outcomes and previously published findings.

Keywords: couple stress nanofluid, mixed convection, MHD, viscous dissipation, ADM, MT, residual error function

1 Introduction

When forced and natural convection occurs together in fluid flow, it is referred to as the mixed convection phenomenon (MCP) [1]. The interaction of these convection types is important in many industrial applications, such as heat exchangers (which maximize heat transfer processes), nuclear reactors (which depend on effective cooling), electronic devices (which improve heat capture), and central solar receivers (which aid in thermal management) [2]. Because it combines the advantages of forced and natural convection, the MCP through nanofluids is very significant because it improves heat transfer efficiency [3].

Flow characteristics are becoming harder to explain in modern engineering when Newtonian fluid models are the only ones used. When it comes to effectively representing flows in a variety of industrial and technical applications, these models frequently fall short in capturing the intricacies and behaviors of real-world fluids, especially those with non-Newtonian features. The theory of non-Newtonian fluids has become extremely helpful and relevant. It is essential for solving problems in contemporary engineering and industrial processes because it offers a more precise framework for simulating and evaluating the intricate flow behaviors seen in many real-world fluids. Non-Newtonian fluids can be categorized into different kinds, such as the power-law model [4], Casson model [5], Bingham plastic model [6], and Carreau model [7], among others. A more accurate representation of the intricate fluid dynamics seen in engineering and industrial contexts is offered by these models, which capture a variety of flow

---

* **Corresponding author: Mohamed Adel,** Department of Mathematics, Faculty of Science, Islamic University of Madinah, Medina, Saudi Arabia, e-mail: adel@sci.cu.edu.eg
Mohamed M. Khader: Department of Mathematics and Statistics, College of Science, Imam Mohammad Ibn Saud Islamic University (IMSIU), Riyadh, Saudi Arabia, e-mail: mmkhader@imamu.edu.sa
Mohamed Messaoudi: Department of Mathematics and Statistics, College of Science, Imam Mohammad Ibn Saud Islamic University (IMSIU), Riyadh, Saudi Arabia, e-mail: mmessaoudi@imamu.edu.sa

behaviors such as shear-thinning, shear-thickening, yield stress, and viscoelastic properties. The models provide for a more accurate understanding and prediction of fluid behavior in processes where classic Newtonian assumptions are inadequate by taking into consideration these various features. Couple stress model [8] is a well-known non-Newtonian fluid model in the literature. It is helpful for analyzing complex flow behaviors in a variety of applications since it incorporates microstructural interactions and rotational effects. The importance of this subject has motivated a great deal of research in a variety of disciplines. Numerous investigations [9–11] and developments in theoretical and practical applications have resulted from its significance in comprehending intricate fluid behaviors.

Khan *et al.* [12] studied the characteristics of micropolar flow in a suction- or injection-driven porous channel, describing the fluid dynamics. The governing nonlinear partial differential equations (PDEs) were reduced to a nonlinear system of ordinary differential equations (ODEs). using similarity variables. The differential transformation method was used to obtain approximate solutions to this system. Khan *et al.* [13] studied the characteristics of micropolar flow in a suction- or injection-driven porous channel, describing the fluid dynamics. The governing nonlinear PDEs were reduced to a nonlinear system of ODEs using similarity variables. The optimal homotopy asymptotic method was used to obtain approximate solutions to this system. Kanwal *et al.* [14] studied the peristaltic flow of dusty fluids, in which dust particles are evenly distributed. This model has a vital role in biomedical sciences and industry. The laws of momentum and energy conservation are used in the mathematical modeling of this problem, and slip conditions are incorporated into both the momentum and thermal properties. The resulting system of coupled equations is solved using the small wavenumber approximation (perturbation technique).

The model under study is limited to a system of highly nonlinear ODEs, and therefore, an exact analytical solution is not possible. Consequently, a robust numerical method is required to approximate the solution effectively. This approach allows us to navigate the model's complexity and derive meaningful numerical results. Additionally, we tackled the issue analytically by employing a novel, recently widened methodology, offering a deeper insight into the solution process. This technique utilizes the modified Adomian decomposition method (MADM), which dislodges the conventional ADM with Mohand transform (MT). This novel strategy represents a substantial advancement in the resolution of challenging analytical items since it supplies increased efficiency and accuracy [15]. Through the application of the MT [16,17], the improved decomposition approach enhances the solution strategy and produces more accurate results for many implementations. The accurate resolution of the problem is aided by a number of solution forms that are obtained from the MADM. Further confirming the efficiency and dependability of this approach is the solution to the ensuing nonlinear system of ODEs. A thorough validation of the scheme is provided through careful analysis and comparison of collected data utilizing tables and charts.

Mahariq *et al.* [18] introduced an effective mathematical model in fractional form for studying the energy transfer from an unsteady flow of an incompressible viscous fluid using radiative heat flux, using the Rosseland discretization and Boussinesq approximations. The model was studied in terms of velocity, temperature, and concentration using statistical approaches. Akhund and Abro [19] presented a conceptual overview of the properties and computational applications of a Newtonian fluid model in its fractional form (fractal-fractional) under exact analytical solutions, using the Sumudu and Laplace transforms. They also compared the solutions and properties with the non-fractional case. They also presented a sensitivity analysis of this model to study the rheological phenomenon using Pearson correlation, regression equations, and potential error. Abro and Atangana [20] studied an important mathematical system within the intrinsic biophysical effects, namely, the reliable neuron model based on Maxwell's electromagnetic induction in its fractional form (several modern definitions of the fractional derivative were used). The cumulative chaotic phenomenon was described and mathematically modeled using Mittag–Leffler kernels of fractional, variable orders. This model was numerically studied using the Adams–Bashforth–Moulton method to obtain an approximate solution.

The aim of this work is to give a novel numerical approach to the nonlinear system of ODEs that characterizes our suggested model. This method seeks to provide a fresh and efficient approach to solving complex nonlinear problems by fusing the MT and ADM. We will consider the impacts of MCP, magnetic field, and viscous dissipation, guaranteeing a thorough examination of these elements and their impact on the system being studied. No prior research has been done on the topic, hence this work constitutes a novel investigation of it.

2 Statement of problem-based on physical formulations

In this study, the behavior of couple stress nanofluid flow over a porous, linearly extending sheet is scrupulous considering the impacts of mixed convection, viscous dissipation, and an applied magnetic field with strength B_0. The output magnetic intensity is taken to be nonexistent or negligible, meaning that its effects are not present in the analysis. The elastic sheet can be stretched by the equation $u = bx$, where b is a constant, and is positioned at the x-axis (Figure 1).

It is thought that the concentration at the wall indicated as C_w (where $C_w > C_\infty$), is uniform. In the meantime, it is presumed that the temperature at the wall T_w follows the formula $T_w = Ax^\lambda + T_\infty$, where A is a constant, T_∞ is the ambient temperature far from the wall, and λ is the exponent of the wall temperature. Since a suction velocity can be created, it is presumed that the sheet is porous. The analysis' representation of this suction velocity, v_w, shows how quickly the fluid is sucked through the sheet's pores. The nanofluid is assumed to have the Brownian diffusion coefficient that is mathematically denoted by D_B and it has a thermophoretic diffusion coefficient that is denoted by D_T. Further, the nanofluid is thought to flow through a porous medium with permeability, denoted mathematically by the symbol k. This property, known as permeability, describes how easily a fluid can pass through a porous structure. These presumptions allow us to write the following governing equations for the current problem [9,21]:

$$u_x + v_y = 0, \tag{1}$$

$$\begin{aligned}(u, v)\cdot\nabla u + \frac{\delta}{\rho}\frac{\partial^4 u}{\partial y^4} = \nu\frac{\partial^2 u}{\partial y^2} + g\beta_t(T - T_\infty) - \frac{\sigma B_0^2}{\rho}u \\ - \frac{\mu}{\rho k}u + g\beta_c(C - C_\infty),\end{aligned} \tag{2}$$

$$\begin{aligned}(u, v)\cdot\nabla T = \frac{\kappa}{\rho c_p}\frac{\partial^2 T}{\partial y^2} + \frac{\nu}{c_p}\left(\frac{\partial u}{\partial y} - \frac{\delta}{\mu\rho}\left(\frac{\partial^3 u}{\partial y^3}\right)\right)\left(\frac{\partial u}{\partial y}\right) \\ + \omega\left(D_B\frac{\partial C}{\partial y} + \frac{D_T}{T_\infty}\frac{\partial T}{\partial y}\right)\left(\frac{\partial T}{\partial y}\right),\end{aligned} \tag{3}$$

$$(u, v)\cdot\nabla C - \frac{D_T}{T_\infty}\frac{\partial^2 T}{\partial y^2} = D_B\frac{\partial^2 C}{\partial y^2}, \tag{4}$$

where the ratio between the micro-particles and the base fluid's heat capacity is denoted by ω. σ is the base fluid's electrical conductivity, and ν is the kinematic viscosity. Also, the amount that a material expands when heated is measured by its coefficient of thermal expansion β_t, while β_c represents the concentration expansion coefficient, which quantifies the extent to which a material's concentration changes in response to variations in its surroundings. Likewise, the specific heat at constant pressure is denoted by c_p. Interestingly, the non-Newtonian couple stress model may be converted to a Newtonian model by setting the material couple stress coefficient ($\delta = 0$) to zero. Furthermore, in order to correctly depict the behavior of the double-stressed nanofluid model within the system, the following boundary conditions (BCs) must be met [9]:

$$\begin{aligned}u = bx,\quad \frac{\partial^2 u}{\partial y^2} = 0,\quad v = -v_w,\quad T = T_w \\ = Ax^\lambda + T_\infty,\quad C = C_w,\quad \text{at } y = 0,\end{aligned} \tag{5}$$

$$u \to 0,\quad \frac{\partial u}{\partial y} \to 0,\quad T \to T_\infty,\quad C \to C_\infty, \text{at } y \to \infty. \tag{6}$$

2.1 Dimensionless form of the model

The previous model can be made simpler by using dimensionless transformations. This method reduces the number of independent variables, which reduces the complexity of the problem and makes the solution process easier to handle and more efficient. This leads to the transformation of the model with its partial differential equation nature into a dimensionless system of ODEs. The transformations

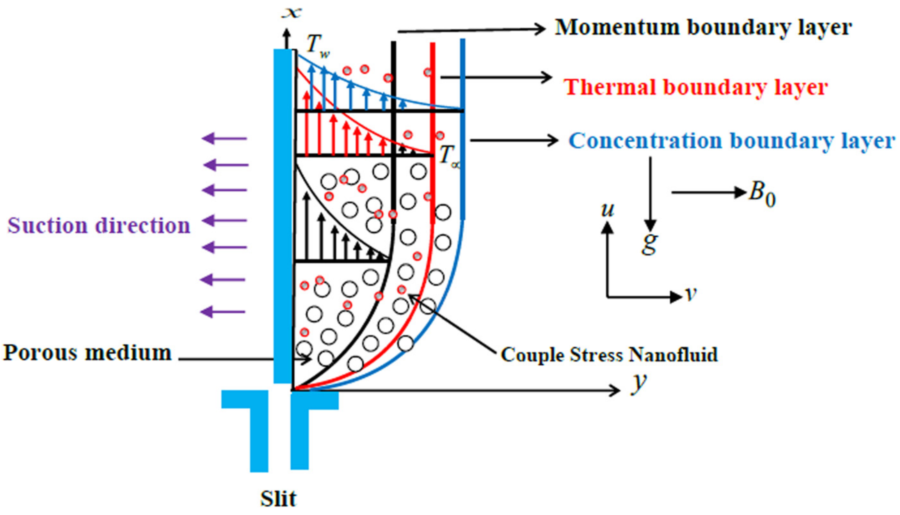

Figure 1: Geometry of couple stress fluid flow.

simplify the equations, which facilitates their analysis and solution and can be characterized as [10]

$$\eta = \left(\frac{b}{\nu}\right)^{\frac{1}{2}} y, \quad u = u_w f'(\eta), \quad \theta = \frac{T - T_\infty}{T_w - T_\infty}, \quad \phi = \frac{C - C_\infty}{C_w - C_\infty}, \quad v = -(b\nu)^{\frac{1}{2}} f(\eta). \tag{7}$$

The model is given as a system of ODEs and the necessary BCs are included in the system that follows. The dimensionless transformations previously described in Eq. (7) were applied to derive these equations. Understanding and advancing the research depend on their formulation

$$\beta f^{(5)} - f''' - ff'' + f'^2 + Mf' + \Lambda f' - \Omega_t\theta - \Omega_c\phi = 0, \tag{8}$$

$$\theta'' + \mathrm{PrEc}(f'' - \beta f^{(4)})f'' + \mathrm{Pr}(f\theta' - \lambda f'\theta) + \mathrm{Pr}(\Gamma_b\phi' + \Gamma_t\theta')\theta' = 0, \tag{9}$$

$$\Gamma_b\phi'' + \Gamma_t\theta'' + \Gamma_b\mathrm{Le}f\phi' = 0. \tag{10}$$

Together with the following related BCs

$$f = \Upsilon, \quad f' = 1, \quad \theta = 1, \quad \phi = 1, \quad f''' = 0, \quad \text{at } \eta = 0, \tag{11}$$

$$f' \to 0, \quad \theta \to 0, \quad \phi \to 0, \quad f'' \to 0, \quad \text{as } \eta \to \infty. \tag{12}$$

In the previously mentioned and most recent system that governs our physical model, the thermal expansion coefficient Ω_t, the magnetic field parameter M, concentration expansion coefficient Ω_c, suction parameter Υ, Eckert number Ec, dimensionless couple stress parameter β, Brownian motion parameter Γ_b, Prandtl number Pr, porous parameter Λ, thermophoresis parameter Γ_t, and Lewis number Le are provided below:

$$\Omega_t = \frac{g\beta(T_w - T_\infty)x^3}{\nu^2}, \quad M = \frac{\sigma}{\rho b}B_0^2, \quad \Omega_c = \frac{g\beta(C_w - C_\infty)x^3}{\nu^2}, \quad \Upsilon = \frac{-v_w}{\sqrt{\nu b}}, \quad \beta = \frac{\delta b}{\nu^2\rho}, \tag{13}$$

$$\mathrm{Ec} = \frac{u_w^2}{c_p(T_w - T_\infty)}, \quad \Gamma_b = \frac{\omega(C_w - C_\infty)D_B}{\nu}, \quad \Lambda = \frac{\nu}{bk}, \quad \mathrm{Pr} = \frac{\mu c_p}{\kappa}, \tag{14}$$

$$\Gamma_t = \frac{\omega(T_w - T_\infty)D_T}{\nu T_\infty}, \quad \mathrm{Le} = \frac{\nu}{D_B}. \tag{15}$$

As stated below, the local skin friction coefficient Cf_x, the Sherwood number Sh_x, and the Nusselt number Nu_x are the three important physical quantities in the current flow analysis

$$\mathrm{Cf}_x\mathrm{Re}^{\frac{1}{2}} = -(f''(\eta) - \beta f^{(4)}(\eta))_{\eta=0}, \quad \mathrm{Sh}_x\mathrm{Re}^{\frac{-1}{2}} = -\phi'(\eta)_{\eta=0}, \quad \mathrm{Nu}_x\mathrm{Re}^{\frac{-1}{2}} = -\theta'(\eta)_{\eta=0}, \tag{16}$$

where $\mathrm{Re} = \frac{u_w x}{\nu}$ is the local Reynolds number.

3 Investigation for solutions of the model

3.1 Basic concepts on the MT

The MT of the function $g(\eta)$ is denoted and given as follows [16]:

$$\mathbb{M}\{g(\eta)\} = G(\varrho) = \varrho^2\int_0^\infty g(\eta)e^{-\varrho\eta}\mathrm{d}\eta, \quad k_1 \le \varrho \le k_2.$$

The inverse MT of $G(\varrho)$ is $\mathbb{M}^{-1}\{G(\varrho)\} = g(\eta)$.

The main properties of the MT [22] are as follows:

- For arbitrary constants a_1, a_2, we have
$$\mathbb{M}\{a_1g_1(\eta) + a_2g_2(\eta)\} = a_1\mathbb{M}\{g_1(\eta)\} + a_2\mathbb{M}\{g_2(\eta)\}.$$
- The MT of the derivatives $g^{(n)}(\eta)$.
$$\mathbb{M}\{g^{(n)}(\eta)\} = \varrho^nG(\varrho) - \varrho^{n+1}g(0) - \varrho^ng'(0) - \ldots - \varrho^2g^{(n-1)}(0), \quad n = 1, 2, \ldots. \tag{17}$$
- The MT for the power functions
$$\mathbb{M}\{\eta^n\} = \begin{cases} \dfrac{n!}{\varrho^{n-1}}, & n \in \mathbb{N}; \\ \dfrac{\Gamma(n+1)}{\varrho^{n-1}}, & n > -1. \end{cases}$$

3.2 Utilizing the MADM

To implement the MADM in the given system (8)–(12), it will be rewritten in the following operator form:

$$f^{(5)}(\eta) = \mathrm{NL}_1(f, \theta, \phi) = \beta^{-1}[f''' + ff'' - f'^2 - (M + \Lambda)f' + \Omega_t\theta + \Omega_c\phi], \tag{18}$$

$$\theta''(\eta) = \mathrm{NL}_2(f, \theta, \phi) = \mathrm{PrEc}(\beta f^{(4)} - f'')f'' + \mathrm{Pr}(\lambda f'\theta - f\theta') - \mathrm{Pr}(\Gamma_b\phi' + \Gamma_t\theta')\theta', \tag{19}$$

$$\phi''(\eta) = \mathrm{NL}_3(f, \theta, \phi) = -(\Gamma_t/\Gamma_b)\theta'' - \mathrm{Le}f\phi'. \tag{20}$$

Take the MT of model (18)–(20) as follows:

$$\begin{aligned} &s^5F(s) - s^6f(0) - s^5f'(0) - s^4f''(0) - s^3f'''(0)\\ &\quad - s^2f^{(4)}(0) = \mathbb{M}[\mathrm{NL}_1(f, \theta, \phi)], \end{aligned} \tag{21}$$

$$s^2\Theta(s) - s^3\theta(0) - s^2\theta'(0) = \mathbb{M}[\mathrm{NL}_2(f, \theta, \phi)], \tag{22}$$

$$s^2\Phi(s) - s^3\phi(0) - s^2\phi'(0) = \mathbb{M}[\mathrm{NL}_3(f, \theta, \phi)]. \tag{23}$$

We can solve the above algebraic system after using BCs (11) and (12):

$$F(s) = s\Upsilon + 1 + \frac{1}{s}\ell_1 + \frac{1}{s^3}\ell_2 + \frac{1}{s^5}\mathbb{M}[\mathrm{NL}_1(f, \theta, \phi)], \tag{24}$$

$$\Theta(s) = s + \ell_3 + \frac{1}{s^2}\mathbb{M}[\mathrm{NL}_2(f, \theta, \phi)], \tag{25}$$

$$\Phi(s) = s + \ell_4 + \frac{1}{s^2}\mathbb{M}[\mathrm{NL}_3(f, \theta, \phi)]. \tag{26}$$

By operating the inverse MT of Eqs (24)–(26), we can obtain

$$\begin{aligned} f(\eta) &= \Upsilon + \eta + \frac{1}{2}\ell_1\eta^2 + \frac{1}{24}\ell_2\eta^4\\ &\quad + \mathbb{M}^{-1}\left[\frac{1}{s^5}\mathbb{M}[\mathrm{NL}_1(f, \theta, \phi)]\right], \end{aligned} \tag{27}$$

$$\theta(\eta) = 1 + \ell_3\eta + \mathbb{M}^{-1}\left[\frac{1}{s^2}\mathbb{M}[\mathrm{NL}_2(f, \theta, \phi)]\right], \tag{28}$$

$$\phi(\eta) = 1 + \ell_4\eta + \mathbb{M}^{-1}\left[\frac{1}{s^2}\mathbb{M}[\mathrm{NL}_3(f, \theta, \phi)]\right], \tag{29}$$

where ℓ_i, $i = 1, 2, 3, 4$ are defined as follows:

$$\ell_1 = f''(0), \quad \ell_2 = f^{(4)}(0), \quad \ell_3 = \theta'(0), \quad \ell_4 = \phi'(0),$$

these quantities ℓ_i, $i = 1, 2, 3, 4$ will be found later by imposing the given BCs (11)–(12).

Now, the components of the approximate solution to the problem under study will be obtained using the iterative scheme as follows:

$$\begin{aligned} f_0(\eta) &= \Upsilon + \eta + \frac{1}{2}\ell_1\eta^2 + \frac{1}{24}\ell_2\eta^4,\\ \theta_0(\eta) &= 1 + \ell_3\eta,\\ \phi_0(\eta) &= 1 + \ell_4\eta, \end{aligned} \tag{30}$$

$$\begin{aligned} f_{m+1}(\eta) &= \mathbb{M}^{-1}\left[\frac{1}{s^5}\mathbb{M}[\mathrm{NL}_1(f, \theta, \phi)]\right] = \mathbb{M}^{-1}\left[\frac{1}{s^5}\mathbb{M}[A_{1,m}]\right],\\ \theta_{m+1}(\eta) &= \mathbb{M}^{-1}\left[\frac{1}{s^2}\mathbb{M}[\mathrm{NL}_2(f, \theta, \phi)]\right] = \mathbb{M}^{-1}\left[\frac{1}{s^2}\mathbb{M}[A_{2,m}]\right],\\ \phi_{m+1}(\eta) &= \mathbb{M}^{-1}\left[\frac{1}{s^2}\mathbb{M}[\mathrm{NL}_3(f, \theta, \phi)]\right] = \mathbb{M}^{-1}\left[\frac{1}{s^2}\mathbb{M}[A_{3,m}]\right]. \end{aligned} \tag{31}$$

We decompose the nonlinear terms $\mathrm{NL}_k(f, \theta, \phi)$, $k = 1, 2, 3$ by utilizing Adomian's polynomials in the following form:

$$\mathrm{NL}_k(f, \theta, \phi) = \sum_{m=0}^{\infty} A_{k,m}, \; k = 1, 2, 3, \tag{32}$$

where,

$$\begin{aligned} A_{k,m} &= \frac{1}{m!}\left[\frac{d^m}{d\chi^m}\left[\mathrm{NL}_k\left(\sum_{i=0}^{\infty}\chi^i f_i, \sum_{i=0}^{\infty}\chi^i\theta_i, \sum_{i=0}^{\infty}\chi^i\phi_i\right)\right]\right]_{\chi=0},\\ k &= 1, 2, 3. \end{aligned} \tag{33}$$

Applying the previous formula, we calculate the first $A_{k,m}$, $k = 1, 2, 3$ in the following form:

$$\begin{aligned} A_{1,0} &= \beta^{-1}[f_0''' + f_0f_0'' - f_0'^2 - (M + \Lambda)f_0' + \Omega_t\theta_0 + \Omega_c\phi_0]\\ &= \beta^{-1}\left[\ell_2\eta + \left(\Upsilon + \eta + \frac{1}{2}\ell_1\eta^2 + \frac{1}{24}\ell_2\eta^4\right)\left(\ell_1 + \frac{1}{2}\ell_2\eta^2\right)\right.\\ &\quad - \left(1 + \ell_1\eta + \frac{1}{6}\ell_2\eta^3\right)^2 - (M + \Lambda)\left(1 + \ell_1\eta\right.\\ &\quad \left.\left. + \frac{1}{6}\ell_2\eta^3\right) + \Omega_t(1 + \ell_3\eta) + \Omega_c(1 + \ell_4\eta)\right], \end{aligned} \tag{34}$$

$$\begin{aligned} A_{1,1} &= \beta^{-1}[f_1''' + f_0f_1'' + f_1f_0'' - 2f_0'f_1' - (M + \Lambda)f_1'\\ &\quad + \Omega_t\theta_1 + \Omega_c\phi_1], \ldots, \end{aligned}$$

$$\begin{aligned} A_{2,0} &= \mathrm{PrEc}(\beta f_0^{(4)} - f_0'')f_0'' + \Pr(\lambda f_0'\theta_0 - f_0\theta_0')\\ &\quad - \Pr(\Gamma_b\phi_0' + \Gamma_t\theta_0')\theta_0'\\ &= \Pr\left(\mathrm{Ec}(\beta\ell_2 - (\ell_1 + 0.5\ell_2\eta^2))(\ell_1 + 0.5\ell_2\eta^2)\right.\\ &\quad + \lambda(1 + \ell_3\eta)\left(1 + \ell_1\eta + \frac{1}{6}\ell_2\eta^3\right) - \ell_3\left(\Upsilon + \eta\right.\\ &\quad \left.\left. + \frac{1}{2}\ell_1\eta^2 + \frac{1}{24}\ell_2\eta^4\right) - (\Gamma_b\ell_4 + \Gamma_t\ell_3)\ell_3\right), \end{aligned} \tag{35}$$

$$\begin{aligned} A_{2,1} &= \mathrm{PrEc}(\beta f_1^{(4)} - f_1'')f_0'' + \mathrm{PrEc}(\beta f_0^{(4)} - f_0'')f_1''\\ &\quad + \Pr\lambda(f_1'\theta_0 + f_0'\theta_1) - \Pr(f_1\theta_0' + f_0\theta_1')\\ &\quad - \Pr(\Gamma_b\phi_1' + \Gamma_t\theta_1')\theta_0' - \Pr(\Gamma_b\phi_0' + \Gamma_t\theta_0')\theta_1', \ldots, \end{aligned}$$

$$\begin{aligned} A_{3,0} &= -(\Gamma_t/\Gamma_b)\theta_0'' - \mathrm{Le}f_0\phi_0'\\ &= -\mathrm{Le}\ell_4\left(\Upsilon + \eta + \frac{1}{2}\ell_1\eta^2 + \frac{1}{24}\ell_2\eta^4\right), \end{aligned} \tag{36}$$

$$A_{3,1} = -(\Gamma_t/\Gamma_b)\theta_1'' - \mathrm{Le}(f_1\phi_0' + f_0\phi_1'), \ldots.$$

We can calculate the first component of the approximate solution using the iterative formula (31) in the following form:

$$\begin{aligned} f_1(\eta) &= \mathbb{M}^{-1}\left[\frac{1}{s^5}\mathbb{M}[A_{1,0}]\right],\\ \theta_1(\eta) &= \mathbb{M}^{-1}\left[\frac{1}{s^2}\mathbb{M}[A_{2,0}]\right],\\ \phi_1(\eta) &= \mathbb{M}^{-1}\left[\frac{1}{s^2}\mathbb{M}[A_{3,0}]\right]. \end{aligned} \tag{37}$$

Thus, we can obtain the approximate solution by collecting m of these approximated terms as follows:

$$
\begin{aligned}
f(\eta) \simeq f_m(\eta) = \sum_{k=0}^{m-1} f_k(\eta), \quad \theta(\eta) \simeq \theta_m(\eta) \\
= \sum_{k=0}^{m-1} \theta_k(\eta), \quad \phi(\eta) \simeq \phi_m(\eta) = \sum_{k=0}^{m-1} \phi_k(\eta),
\end{aligned}
\tag{38}
$$

when $m \to \infty$, this form is close to the true solution.

The values of $\ell_i, i = 1, 2, 3$ will be given by applying the BCs (11) and (12).

To attain a complete numerical investigation, we estimate the residual error function $\text{REF}_f(m, \eta)$, $\text{REF}_\theta(m, \eta)$, $\text{REF}_\phi(m, \eta)$ [23] for the solution $f(\eta), \theta(\eta)$, and $\phi(\eta)$, respectively, of Eqs. (8)–(10) as follows:

$$
\begin{aligned}
\text{REF}_f(m, \eta) = \beta f_m^{(5)}(\eta) - f_m'''(\eta) - f_m(\eta) f_m''(\eta) + f_m'^2(\eta) \\
+ M f_m'(\eta) + \Lambda f_m'(\eta) - \Omega_t \theta_m(\eta) \\
- \Omega_c \phi_m(\eta) \simeq 0,
\end{aligned}
\tag{39}
$$

$$
\begin{aligned}
\text{REF}_\theta(m, \eta) = \theta_m''(\eta) + \Pr\text{Ec}(f_m''(\eta) - \beta f_m^{(4)}(\eta)) f_m''(\eta) \\
+ \Pr(f_m(\eta)\theta_m'(\eta) - \lambda f_m'(\eta)\theta_m(\eta)) \\
+ \Pr(\Gamma_b \phi_m'(\eta) + \Gamma_t \theta_m'(\eta))\theta_m'(\eta) \simeq 0,
\end{aligned}
\tag{40}
$$

$$
\begin{aligned}
\text{REF}_\phi(m, \eta) = \Gamma_b \phi_m''(\eta) + \Gamma_t \theta_m''(\eta) + \Gamma_b \text{Le} f_m(\eta) \phi_m'(\eta) \\
\simeq 0.
\end{aligned}
\tag{41}
$$

4 Verification of the numerical approach and its precision

The values for Nusselt number $-\theta'(0)$ are examined and contrasted in this section with the values found by Khan and Pop [24] for various Brownian motion parameter Γ_b in Table 1. This comparison demonstrates how accurate and consistent the present findings are. We can see how well this comparison agrees for all values of Γ_b. This reassures us that the existing results are extremely accurate and that the numerical method has been suggested as a reliable and effective procedure to handle this kind of fluid flow problem. All computations in this research were conducted utilizing Mathematica 8.0.

To validate our approximate solutions at $\text{Le} = \lambda = \Upsilon = 1.0$, $\text{Ec} = \beta = M = \Lambda = \Gamma_t = 0.2$, $\Gamma_b = 0.7$, $\Pr = 3.0$, $\Omega_t = 0.5$, $\Omega_c = 0.1$, we give a comparison in Tables 2–4 for $f(\eta), \theta(\eta)$, and $\phi(\eta)$, respectively, with the ADM [25,26] with different values of m by computing the REF in the two methods. This comparison displays the thoroughness of the introduced method in this work. The error-REF reduction and accuracy of the method can be controlled by choosing appropriate values for the approximation order m.

Table 1: Variation of $-\theta'(0)$ against Γ_b with $\Upsilon = \text{Ec} = M = \Lambda = \Omega_t = \beta = \Omega_c = \lambda = 0$, $\Gamma_t = 0.3$, and $\Pr = 10$

Γ_b	**Work [24]**	**Current results**
0.5	0.0291	0.028997880
0.4	0.0641	0.063990218
0.3	0.1355	0.135477089
0.2	0.2731	0.272998074
0.1	0.5201	0.520079982

5 Results and discussion

We show graphically each of the temperature, velocity, and concentration profiles, which were obtained by combining the Adomian decomposition approach with the Mohand transform. These illustrations provide a more in-depth understanding of the fluid flow's behavior and properties under different circumstances. Figure 2 shows how the concentration, temperature, and velocity amplitudes are affected by the thermal expansion parameter Ω_t. This graph shows that the velocity amplitude increases with the values of the thermal expansion parameter. But it

Table 2: Comparison of the REF between the MADM and ADM *via* various quantities of m

	MADM−REF$_f$ at		**ADM−REF$_f$ at**	
η	$m = 6$	$m = 12$	$m = 6$	$m = 12$
0	9.25×10^{-7}	3.65×10^{-11}	4.02×10^{-5}	3.26×10^{-7}
0.6	9.25×10^{-6}	8.24×10^{-9}	3.29×10^{-3}	5.21×10^{-7}
1.2	7.26×10^{-6}	6.53×10^{-9}	2.65×10^{-5}	6.33×10^{-6}
1.8	6.02×10^{-6}	5.32×10^{-9}	9.01×10^{-3}	6.26×10^{-5}
2.4	9.26×10^{-6}	2.40×10^{-9}	7.37×10^{-3}	7.23×10^{-5}
3	6.23×10^{-5}	2.15×10^{-9}	7.45×10^{-3}	6.26×10^{-5}

Table 3: Comparison of the REF between the MADM and ADM *via* various quantities of m

	MADM−REF$_\theta$ at		**ADM−REF$_\theta$ at**	
η	$m = 6$	$m = 12$	$m = 6$	$m = 12$
0	5.00×10^{-7}	9.26×10^{-9}	3.67×10^{-4}	3.26×10^{-7}
0.6	7.26×10^{-6}	5.24×10^{-9}	9.26×10^{-4}	5.29×10^{-6}
1.2	8.03×10^{-6}	2.02×10^{-10}	2.01×10^{-3}	2.60×10^{-8}
1.8	7.03×10^{-6}	1.48×10^{-11}	6.10×10^{-3}	9.26×10^{-6}
2.4	7.26×10^{-6}	7.65×10^{-8}	2.02×10^{-3}	2.31×10^{-6}
3	6.03×10^{-5}	7.01×10^{-8}	6.20×10^{-3}	2.30×10^{-5}

Table 4: Comparison of the REF between the MADM and ADM *via* various quantities of m

	MADM−REF$_\phi$ at		**ADM−REF$_\phi$ at**	
η	$m = 6$	$m = 12$	$m = 6$	$m = 12$
0	7.26×10^{-6}	6.26×10^{-9}	6.26×10^{-4}	7.26×10^{-7}
0.6	8.27×10^{-5}	7.56×10^{-10}	9.01×10^{-4}	2.59×10^{-8}
1.2	9.03×10^{-6}	2.59×10^{-10}	7.20×10^{-3}	2.94×10^{-6}
1.8	2.50×10^{-5}	7.01×10^{-9}	7.26×10^{-4}	9.26×10^{-6}
2.4	8.06×10^{-6}	2.23×10^{-9}	2.26×10^{-3}	8.25×10^{-5}
3	6.00×10^{-5}	3.25×10^{-8}	6.03×10^{-3}	5.27×10^{-5}

also results in a simultaneous drop in $\theta(\eta)$ and $\phi(\eta)$. This offers that as Ω_t increases, there is a trade-off between the fluid's velocity and its temperature and concentration distributions. Physically, the buoyancy force in the model, which is brought on by the MCP, is responsible for the boost in velocity.

Figure 3 shows how the solution domain is affected by the concentration expansion parameter Ω_c. The concentration expansion parameter improves the velocity $f'(\eta)$ greatly away from the wall, but it also significantly reduces $\theta(\eta)$ and $\phi(\eta)$. This can be attributed to the expansion parameter's enhanced diffusion rates, which speed up fluid motion and encourage the temperature and concentration boundary layers (BLs) to thin. The fluid's capacity to transmit mass and heat is thereby diminished, resulting in lower concentration and temperature profiles.

In Figure 4, the couple stress nanofluid flow characteristics are affected by M. This parameter introduces a resistive force that interacts with the couple stress properties of the nanofluid, causing significant changes in the fluid dynamics, including $\theta(\eta)$, $\phi(\eta)$, and $f'(\eta)$. It is evident that when M increases, the velocity's amplitude decreases, and the opposite trend appears for the coupling stress nanofluid concentration and temperature. Reduced velocity and higher heat dissipation in the fluid are the results

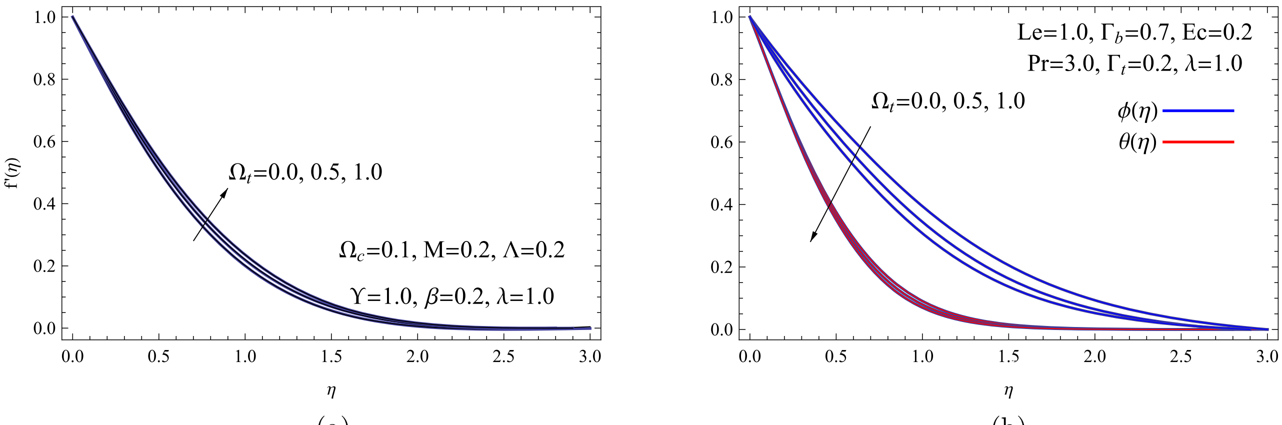

(a) (b)

Figure 2: (a) $f'(\eta)$ for assorted Ω_t and (b) $\theta(\eta)$ and $\phi(\eta)$ for assorted Ω_t.

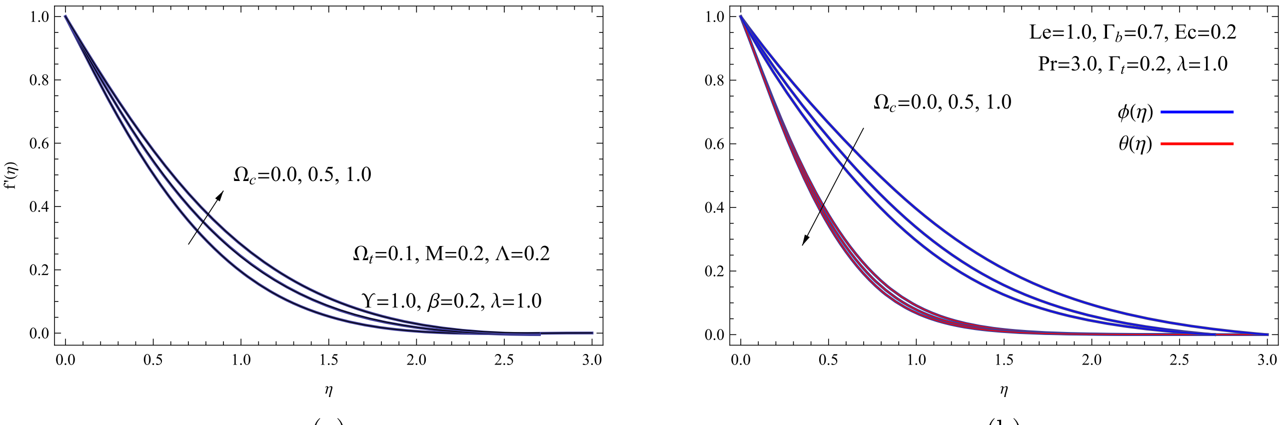

(a) (b)

Figure 3: (a) $f'(\eta)$ for assorted Ω_c and (b) $\theta(\eta)$ and $\phi(\eta)$ for assorted Ω_c.

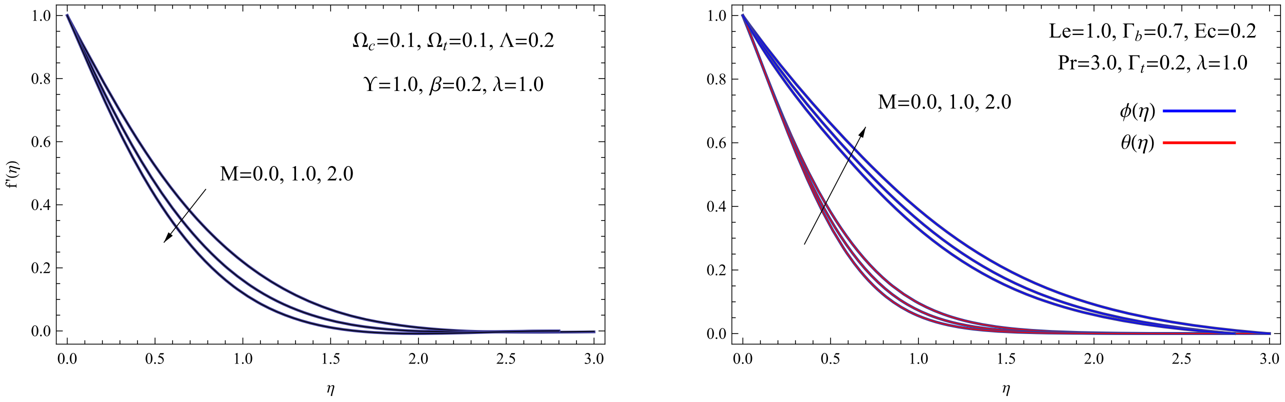

(a) (b)

Figure 4: (a) $f'(\eta)$ for assorted M and (b) $\theta(\eta)$ and $\phi(\eta)$ for assorted M.

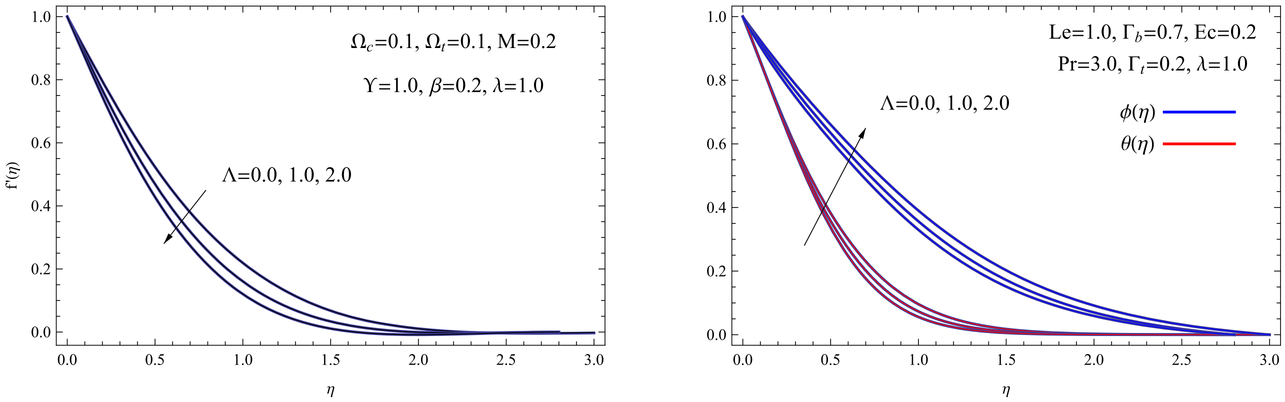

(a) (b)

Figure 5: (a) $f'(\eta)$ for assorted Λ and (b) $\theta(\eta)$ and $\phi(\eta)$ for assorted Λ.

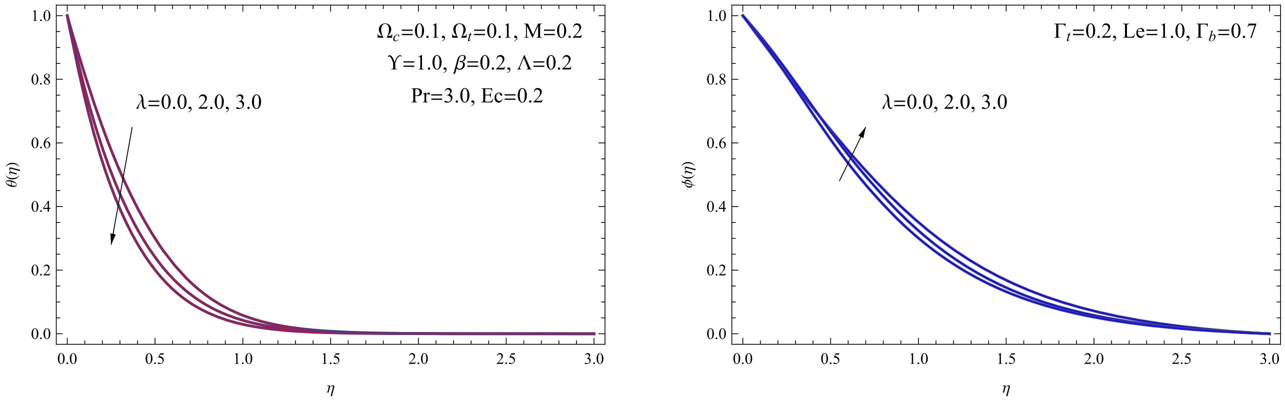

(a) (b)

Figure 6: (a) $\theta(\eta)$ for assorted λ and (b) $\phi(\eta)$ for assorted λ.

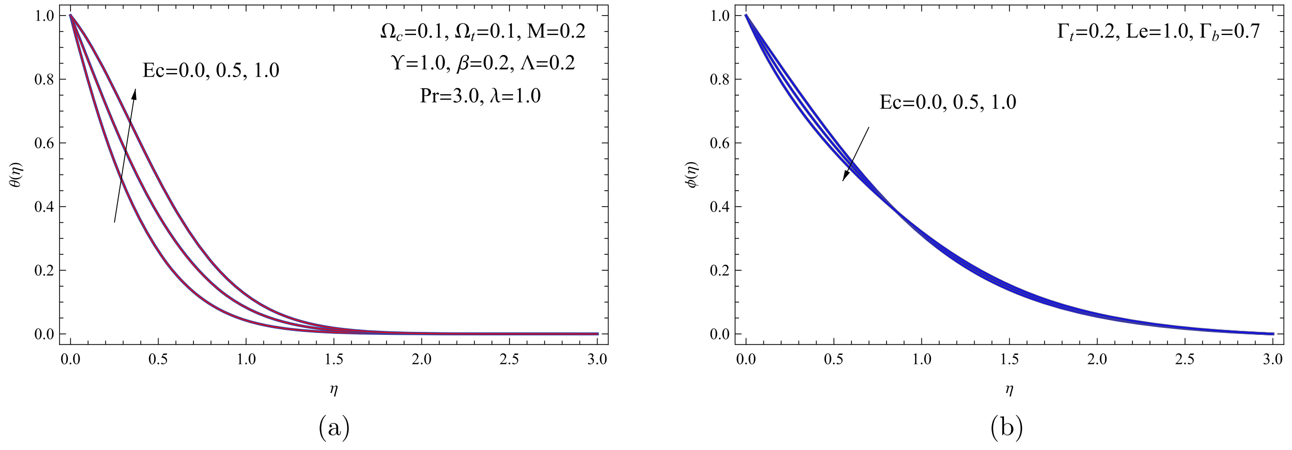

(a) (b)

Figure 7: (a) $\theta(\eta)$ for assorted Ec and (b) $\phi(\eta)$ for assorted Ec.

Table 5: $\mathrm{Sh}_x\mathrm{Re}^{\frac{-1}{2}}$, $\mathrm{Nu}_x\mathrm{Re}^{\frac{-1}{2}}$, and $\mathrm{Cf}_x\mathrm{Re}^{\frac{1}{2}}$ values as function of specific governing parameters with $\mathrm{Pr} = 3.0$, $\mathrm{Le} = 1.0$, $\beta = 0.2$, $\Gamma_b = 0.7$, $\Gamma_t = 0.2$, and $\Upsilon = 1.0$

Ω_t	Ω_c	M	Λ	λ	Ec	$\mathrm{Cf}_x\mathrm{Re}^{\frac{1}{2}}$	$\mathrm{Nu}_x\mathrm{Re}^{\frac{-1}{2}}$	$\mathrm{Sh}_x\mathrm{Re}^{\frac{-1}{2}}$
0.0	0.1	0.2	0.2	1.0	0.2	1.84110	1.46017	0.769252
0.5	0.1	0.2	0.2	1.0	0.2	1.66553	1.46351	0.900485
1.0	0.1	0.2	0.2	1.0	0.2	1.49909	1.46689	1.017123
0.1	0.0	0.2	0.2	1.0	0.2	1.86158	1.45352	0.763014
0.1	0.5	0.2	0.2	1.0	0.2	1.59192	1.48133	0.908501
0.1	1.0	0.2	0.2	1.0	0.2	1.35315	1.50095	1.030782
0.1	0.1	0.0	0.2	1.0	0.2	1.71182	1.45155	1.003220
0.1	0.1	1.0	0.2	1.0	0.2	2.14261	1.42334	0.889382
0.1	0.1	2.0	0.2	1.0	0.2	2.51377	1.36042	0.778145
0.1	0.1	0.2	0.0	1.0	0.2	1.71182	1.45155	1.003220
0.1	0.1	0.2	1.0	1.0	0.2	2.14261	1.42334	0.889382
0.1	0.1	0.2	2.0	1.0	0.2	2.51377	1.36042	0.778145
0.1	0.1	0.2	0.2	0.0	0.2	1.81143	1.98007	0.740195
0.1	0.1	0.2	0.2	2.0	0.2	1.81545	2.59051	0.573093
0.1	0.1	0.2	0.2	3.0	0.2	1.81986	2.99660	0.424228
0.1	0.1	0.2	0.2	1.0	0.0	1.81519	2.20524	0.794047
0.1	0.1	0.2	0.2	1.0	0.5	1.81014	1.43017	1.009481
0.1	0.1	0.2	0.2	1.0	1.0	1.80216	0.66047	1.224301

of the Lorentz force generated by M acting as a resistance force to the flow. Because of the decreased convective transport, this raises $\theta(\eta)$, $\phi(\eta)$ levels and causes the thermal and concentration BLs to get thicker as the magnetic field strength rises.

Figure 5 shows, while holding the other parameters constant, how $f'(\eta)$, $\phi(\eta)$, and $\theta(\eta)$ affect various values of Λ. The attracting body force with the porosity parameter is orientated in the opposite trend of x on the x-axis. Consequently, a larger value for the porous parameter will lead to greater resistance against the axial velocity, which will lower the velocity and improve the concentration and temperature profiles. This happens as a result of the fluid flow being slowed down by the increased resistance, which gives the BL more time to transfer mass heat and produces thicker thermal and concentration BLs.

Retaining all other parameters constant, Figure 6 illustrates the effect of the wall temperature exponent λ on $\theta(\eta)$ and $\phi(\eta)$ fields. The nanofluid temperature is negatively impacted by a surge in the surface temperature parameter; however, the nanofluid concentration is positively impacted. BL thickness decreases, fluid temperature drops, and concentration rises, as the surface temperature parameter rises. The physical explanation for this behavior is because that the fluid's surface has a greater ability to transmit heat, which produces a cooling effect that is more effective. Consequently, the fluid temperature decreases due to a smaller thermal BL, and an increase in solute concentration near the surface is promoted by a compressed concentration BL.

Figure 7 shows how with all other parameters fixed or unchanged, Ec affects a couple stress nanofluids $\theta(\eta)$ and $\phi(\eta)$. Eckert number generally results in a fall in nanofluid concentration, especially close to the sheet surface, and a surge in the temperature field and thermal BL thickness. This is due to the fluid temperature rising as a result of viscous dissipation, which transforms energy from motion into internal energy. Due to the increased temperature, the thermal BL thickens due to enhanced thermal diffusion. Further, greater energy dissipation enhances molecular diffusion and lowers concentration, leading to a thinner concentration boundary layer near the surface.

Table 5 now provides a knowledge of how all controlling parameters affect $\mathrm{Cf}_x\mathrm{Re}^{\frac{1}{2}}$, $\mathrm{Sh}_x\mathrm{Re}^{\frac{-1}{2}}$, and $\mathrm{Nu}_x\mathrm{Re}^{\frac{-1}{2}}$. These numbers allow us to estimate the total heat and mass transfer (HMT) rates, examine the fluid flow's effectiveness, and evaluate the nanofluid's performance in various scenarios. Understanding how various factors impact the rate of the HMT, as well as the frictional forces, is essential for optimizing industrial processes and applications employing nanofluids. Undoubtedly, the skin-friction coefficient's amplitude increases when the magnetic parameter, porous parameter, and wall temperature exponent go up, but it reduces as the thermal and concentration expansion factors improve. Furthermore, by boosting the porous and magnetic field parameters, the same table demonstrates that the local Nusselt number reduces monotonically. It also turns out that as the Eckert number rises, $\mathrm{Sh}_x\mathrm{Re}^{\frac{-1}{2}}$ rises and $\mathrm{Nu}_x\mathrm{Re}^{\frac{-1}{2}}$ falls. On the other hand, the exponent of the wall temperature exhibits the opposite pattern for $\mathrm{Sh}_x\mathrm{Re}^{\frac{-1}{2}}$ and $\mathrm{Nu}_x\mathrm{Re}^{\frac{-1}{2}}$.

6 Conclusion

The authors are aware that no previous studies have explicitly investigated the mixed convection behavior of a couple stress nanofluid flow over a permeable stretching surface in a Darcy porous medium, taking into account both viscous dissipation and magnetic field effects. Because it tackles a unique combination of physical phenomena crucial to different industrial and technical applications, where the interaction of magnetic fields, fluid dissipation, and porous media play a crucial role, this gap in the literature underscores the novelty of the current study. In light of the aforementioned assumptions, the main goal of this work is to simulate the mass, flow, and heat transfer of the couple stress fluid. Utilizing both the ADM and MT, the problem is addressed numerically. Graphs are used to show how different parameters affect the results. This problem's principal conclusions are as follows:

1) At the same time that $\theta(\eta)$ and $\phi(\eta)$ of the nanofluid decreases, both the thermal and concentration expansion parameters cause the velocity to increase.
2) The exponent of the wall temperature causes the temperature to drop, but the Eckert number causes it to rise.
3) The $\theta(\eta)$ and $\phi(\eta)$ increase in response to both the magnetic field and porous parameters, while the nanofluid velocity decreases.
4) A greater function of the porous parameter, the exponent of the wall temperature, and the magnetic field parameter result in an increased drag force. By raising the temperature and concentration expansion parameters, on the other hand, it decreases.
5) Future research could expand this model to better reflect real-world conditions by incorporating 3D flow dynamics, temperature-sensitive material properties, and machine learning algorithms. These enhancements would improve both the precision and computational performance of the solutions.
6) Residual error functions are utilized to verify the accuracy of the derived solutions in the absence of exact solutions. Comparisons with well-established numerical models in the literature were accomplished.
7) In addition, by increasing m, we can control the accuracy and effectiveness of the numerical solutions by using the given computational scheme. The results displayed in the tables and figures validate that the proposed technique is both highly precise and efficient, as well as adept at addressing a range of analogous model challenges.
8) In future work, we will try to study the convergence by presenting a theoretical study to prove it, as well as making further modifications to the proposed method to avoid shortcomings and to increase the accuracy of the solutions and the efficiency of the technique. Also, we try to solve this problem using other methods, such as the finite element method or finite difference method.

Acknowledgments: This work was supported and funded.by the Deanship of Scientific Research at Imam Mohammad Ibn Saud Islamic University (IMSIU) (grant number IMSIUDDRSP2503).

Funding information: This work was supported and funded by the Deanship of Scientific Research at Imam Mohammad Ibn Saud Islamic University (IMSIU) (grant number IMSIU-DDRSP2503).

Author contributions: Mohamed M. Khader: project administration, investigation, funding acquisition, and conceptualization; Mohamed Adel: writing – original draft preparation, methodology, supervision, and formal analysis; Mohamed Messaoudi: writing – review and editing, visualization, and writing – original draft preparation. All authors have accepted responsibility for the entire content of this manuscript and approved its submission.

Conflict of interest: The authors state no conflict of interest.

Data availability statement: All data generated or analysed during this study are included in this published article.

References

[1] Hayat T, Shehzad SA, Ashraf MB, Alsaedi A. Magnetohydrodynamic mixed convection flow of thixotropic fluid with thermophoresis and Joule heating. J Thermophys Heat Transfer. 2013;27:733–40.

[2] Afzal K, Aziz, A. Transport and heat transfer of time-dependent MHD slip flow of nanofluids in solar collectors with variable thermal conductivity and thermal radiation. Results Phys. 2016;6:746–53.

[3] Kumar JP, Umavathi JC, Gireesha, BJ, Prasad MK. Mixed convective flow in a vertical double passage channel filled with nanofluid using Robin boundary conditions. J Nanofluids. 2016;5:549–59.

[4] Megahed AM. Variable viscosity and slip velocity effects on the flow and heat transfer of a power-law fluid over a non-linearly stretching surface with heat flux and thermal radiation. Rheologica Acta. 2012;51:841–74.

[5] Abd El-Aziz M, Afify AA. MHD Casson fluid flow over a stretching sheet with entropy generation analysis and Hall influence. Entropy. 2019;21:592.

[6] Rees DAS, Bassom AP. Unsteady thermal BL flows of a Bingham fluid in a porous medium following a sudden change in surface heat flux. Int J Heat Mass Transfer. 2016;93:1100–6.

[7] Abbas T, Rehman S, Shah RA, Idrees M, Qayyum M. Analysis of MHD Carreau fluid flow over a stretching permeable sheet with variable viscosity and thermal conductivity. Phys A Stat Mech Appl. 2020;551:124225.

[8] Stokes VK. Couple stress fluids. Phys Fluid. 1966;9:1709–15.

[9] Khan NA, Riaz F, Khan NA. Heat transfer analysis for couple stress fluid over a nonlinearly stretching sheet. Nonlinear Eng. 2013;2:121–7.

[10] Khan SU, Shehzad SA, Rauf A, Ali N. Mixed convection flow of couple stress nanofluid over an oscillatory stretching sheet with heat absorption/generation effects. Results Phys. 2018;8:1223–31.

[11] Mkhatshwa MP, Motsa SS, Sibanda P. MHD mixed convection flow of couple stress fluid over an oscillatory stretching sheet with thermophoresis and thermal diffusion using the overlapping multi-domain spectral relaxation approach. Int J Appl Comput Math. 2021;7:93.

[12] Khan A, Ullah S, Shah K, Alqudah MA, Abdeljawad T, Ghani A. Theory and semi-analytical study of micropolar fluid dynamics through a porous channel. Comput Model Eng Sci. 2023;136(2):1473–86.

[13] Khan AA, Zafar S, Khan A, Abdeljawad T. Tangent hyperbolic nanofluid flow through a vertical cone: Unraveling thermal conductivity and Darcy-Forchheimer effects. Modern Phys Lett B. 2025;39(8):2450398:1-16.

[14] Kanwal A, Khan AA, Khan A, Almutairi DK, Abdeljawad T. Entropy generation analysis of dusty fluid with peristalsis in asymmetric channel with slip effects. Fractals. 2024;2440059:1–11.

[15] Khader MM, Hijaz A, Megahed AM. Developing some engineering applications through numerical treatment of non-Newtonian nanofluid flow on nonlinear stretching surface with heat generation. Case Stud Therm Eng. 2023;51:1–12.

[16] Shah R, Farooq U, Khan H, Baleanu D, Kumam P, Arif M. Fractional view analysis of third-order Kortewege-De Vries equations, using a new analytical technique. Front Phys. 2020;7:244.

[17] Sudhanshu A, Rashmi M, Anuj K. A comparative study of Mohand and Elzaki transforms. Global J Eng Sc Res. 2016;6(2):203–13.

[18] Mahariq I, Abro KA, Siyal A. Energy transfer and thermal transport for unsteady fractional viscous fluid under Fourier and statistical analysis. Propulsion Power Res. 2025;14(1):160–72.

[19] Akhund A, Abro KA. Fractal modeling of non-integer Newtonian fluid through comparison of Sumudu and Laplace transforms. Int J Geometr Methods Modern Phys. 2025;22(5):2450328.

[20] Abro KA, Atangana A. Mathematical modeling of neuron model through fractal-fractional differentiation based on Maxwell electromagnetic induction: application to neurodynamics. Neural Comput Appl. 2024;36:18377–85.

[21] Joseph SP. Some exact solutions for incompressible couple stress fluid flow. Malaya J Mat. 2020;1:648–52.

[22] Khader MM, Adel M, Mohammed Messaoudi. Modeling and numerical simulation of Maxwell nanofluid flow with heat generation and convective heating: A combined Adomian decomposition method and Mohand transform. Boundary Value Problems. 2025;66:1–16.

[23] Parand K, Delkhosh M. Operational matrices to solve nonlinear Volterra-Fredholm integro-differential equations of multi-arbitrary order. Gazi Univ J Sci. 2016;29(4):895–907.

[24] Khan WA, Pop I. Boundary-layer flow of a nanofluid past a stretching sheet. Heat Mass Transer. 2010;53:2477–83.

[25] Marliadi S, Nadihah W, Adem K. A fractional model of Abalone growth using Adomian decomposition method. Europ J Pure Appl Math. 2025;18(2):5799.

[26] Javed I, Iqbal S, Ali J, Siddique I, Younas MH. Unveiling the intricacies: analytical insights into time and space fractional order inviscid Burger's equations using the Adomian decomposition method. Partial Differ Equ Appl Math. 2024;11:100817.